Superior Performance of Ca(OH)$_2$-CaO-H$_2$O System Doped with Cerium and Lithium for Thermochemical Energy Storage

Lin Zhu, Ya-Ting Li, Deng-Yu Wang, En-Xu Ren, Zhi-Bin Xu*, Qin-Pei Wu*

School of Chemistry and Chemical Engineering, Beijing Institute of Technology, Beijing, 102488, China

*Corresponding author:

Prof. Dr. Qin-Pei Wu

School of Chemistry and Chemical Engineering,
Beijing Institute of Technology, Beijing 102488, China
E-mail: qpwu@bit.edu.cn

ABSTRACT

Thermochemical energy storage is a next generation technology and also an efficient solution for large-scale use of solar energy. Lime (CaO) doped with cerium nitrate (Ce(NO$_3$)$_3$) and lithium hydroxide (LiOH) has been demonstrated to be an excellent energy storage material via the dehydration-hydration process. The heat–storage rate is massively enhanced, by 173–fold. The dehydration conversion ratio increases by 98% (65.3-fold increase) in 28 min. The cycling stability of Ca(OH)$_2$-Ce(NO$_3$)$_3$-LiOH composites in the process of thermal storage and release has also been greatly improved. The peak temperature of dehydration is reduced significantly from 418 to 341^{0}C. The activation energy and the pre-exponential factor ln$A$ for Ca(OH)$_2$ dehydration decrease by 34.6% and 29.4%, respectively. The crystal parameters and the crystal volume of Ca(OH)$_2$ are enlarged. Particle size and agglomeration are decreased. The kinetic equations for dehydration could be leveraged in future for the purpose of informing reactor design and simulations.

**Keywords:** calcium, hydroxide, cerium, lithium, thermal energy, energy storage

INTRODUCTION

Increased fossil fuel consumption has led to more pollutant emissions and a greater demand for green energy to support sustainability. Solar radiation provides the Earth with a huge amount of green energy; however, a drawback is its intermittent nature [1,2]. A promising resolution to this issue is the application of thermal-energy storage systems [3-5]. Thermal-storage systems can be classified into three types: sensible heat storage, latent heat storage, and thermochemical energy storage (TES) [6,7]. As typical candidates of sensible heat storage, molten salts have been used for energy storage for decades. Thermal loss is a drawback of this technology.[4] Latent heat storage works on the thermal energy of the phase change of materials[3,8]. TES works on reversible endothermic and exothermic reactions to store and release thermal energy

[9,10]. Among these three types, TES technology has markedly advantages, i.e., high energy density and long-term storage with minimal energy loss [3,11]. TES thus makes it possible to offer high grade thermal energy in the winter with the heat stored in the summer [2,12].

Among the various materials for TES [13], lime has promising features for practical application, i.e., low cost, no waste, non-toxicity, good stability, controllable safety, and high energy density. However, the low heat-storage rate, low conversion, and the poor reversibility of heat storage and heat release cannot satisfy practical demands, arising partially from the low permeability and agglomeration of lime and hydrated lime in the cyclic process of charge and discharge [14].

The heat-storage principal of lime can be expressed as

$$Ca(OH)_2(s) + \Delta H \rightleftharpoons CaO(s) + H_2O(g)$$
$$\Delta H = 104.2 \text{ kJ mol}^{-1} \tag{1}$$
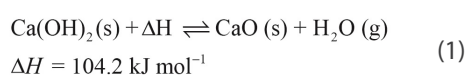
Approaches to mitigating these issues include reactor design [15-17] and modification of heat-storage materials [18]. The latter has been a particular focus in recent years [19]. Shkatulov and co-workers [20,21] reported that both KNO_3 and $LiNO_3$ can accelerate the dehydration of both $Ca(OH)_2$ and $Mg(OH)_2$ and notably reduce the dehydration temperature. The dehydration rate of $Ca(OH)_2$ is improved through reduction of the activation energy by LiOH doping [22]. Huang *et al*. [23] reported that 15 wt% boron nitride improves the thermal conductivity of calcium hydroxide by 20%–30%. CaO granules encapsulated with Al_2O_3 [24] and calcium silicate has be used to improve the cycling stability [25,26]. We have hitherto reported that $ZrO(NO_3)_2$ notably enhances the heat storage rate of $Ca(OH)_2$ [27]. However, materials with high heat-storage performance are still required. Herein, we report the exceptional effect of $Ce(NO_3)_3$-LiOH on enhancing $Ca(OH)_2$ heat storage via reducing both the activation energy of dehydration and the agglomeration and increasing the permeability.

EXPERIMENTAL DESIGN

Material preparation

$Ca(OH)_2$ with a purity of 98% was prepared via a purification procedure as described previously (Supplementary Information (SI), Fig. 1). Composites of $Ca(OH)_2$ with various contents of $Ce(NO_3)_3$ and LiOH are termed CaCeLi-*x*-*y* where *x* and *y* are the mass percentages of $Ce(NO_3)_3$ and LiOH in composites, respectively (Table 1). Under a nitrogen atmosphere, the composites were prepared by mixing $Ca(OH)_2$ with aqueous solutions of $Ce(NO_3)_3$ (98.0%, Innochem, Ltd.,

Beijing) through a 200-mesh sieve. The mixture was stirred for 2 h, evaporated under reduced pressure to remove the solvent, and then dried at 120 °C for 2 h under vacuum. The solid was then mixed with a methanol solution of LiOH (98%) with ultrasonic dispersion for 1 h. After removal of the solvent, the dried composites were sealed for subsequent analysis.

Table 1: Composites of $Ca(OH)_2$ with various contents of $Ce(NO_3)_3$ and LiOH

Composite symbol (CaCeLi-x-y)	Additive and its mass percentage
CaCe-10	$Ce(NO_3)_3$, 10%
CaLi-10	LiOH, 10%
CaCeLi-3-5	$Ce(NO_3)_3$, 3%; LiOH, 5%
CaCeLi-5-10	$Ce(NO_3)_3$, 5%; LiOH, 10%
CaCeLi-10-10	$Ce(NO_3)_3$, 10%; LiOH, 10%

Reversibility of heat storage and release

The reversibility of heat storage and release was evaluated using 5.0 g of dried samples. Samples first underwent dehydration at 310 °C for 100 min to complete heat storage and then cooled to ca 50 °C while sealed. Degassed deionised water was added to finish the corresponding hydration and thus one dehydration–hydration cycle is performed. This procedure was repeated 30 times. Some samples were collected from the hydration products for analysis after 1, 5, 10, 15, 20, 25, and 30 cycles. Isothermal dehydration TG methods were used to evaluate the reversibility. The temperature quickly rises to 310 °C and is maintained for 300 min to generate a mass loss curve with a thermogravimetric analyser, which is then transferred to the conversion curves. The largest conversion (α_{max}) and the corresponding maximal conversion-times (t_{max}) are derived. The higher αmax accords to the higher reversibility of the heat storage and release.

RESULTS AND DISCUSSION

Heat-storage thermodynamics

Differential scanning calorimetry (DSC) and thermogravimetric analysis (TGA) technology was employed to investigate the effects of $Ce(NO_3)_3$ and LiOH on the thermodynamics and kinetics of $Ca(OH)_2$ dehydration. The endothermic dehydration processes of various CaCeLi-*x*-*y* composites and pure $Ca(OH)_2$ were recorded at 10 °C/min (Fig. 1a). Among these DSC curves, one big endothermic-peak is observed and all the peaks of

CaCeLi-*x-y* shift down to much lower temperature than that for pure Ca(OH)$_2$. Two endothermic peaks are observed in the DSC curves for CaCe-10 and CaLi-10. These two small peaks should be given by the decomposition of Ce(NO$_3$)$_3$ and LiOH, respectively (SI, Figs. 2 and 3). All the dehydration onset-, peak-, and end-temperatures (T_{onset}, T_{peak}, and T_{end}) are significantly diminished. CaCeLi-10-10 shows the largest reduction among these composites, specifically 57 °C, 77 °C, and 68 °C for T_{onset}, T_{peak}, and T_{end}, respectively (Fig. 1b). Low dehydration temperature is an advantage in practical application [28]. Meanwhile, the trends indicate that these reductions increase with increasing contents of the additives.
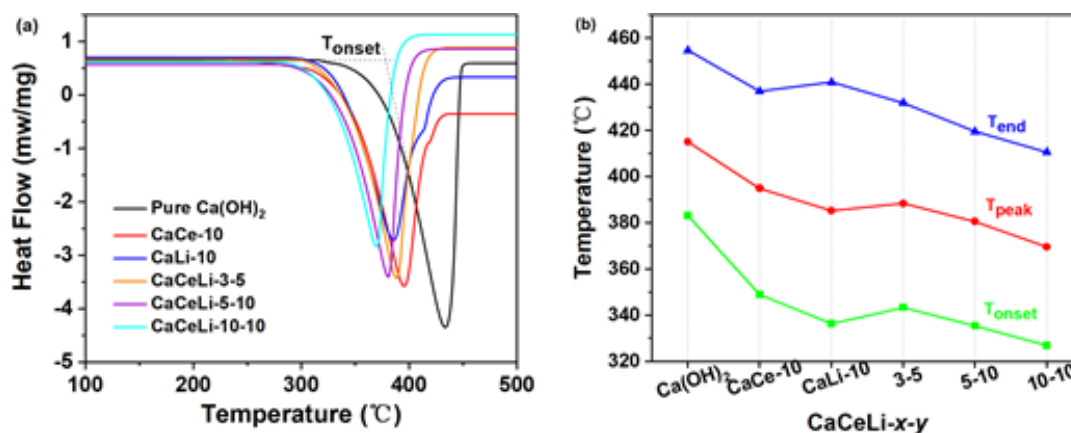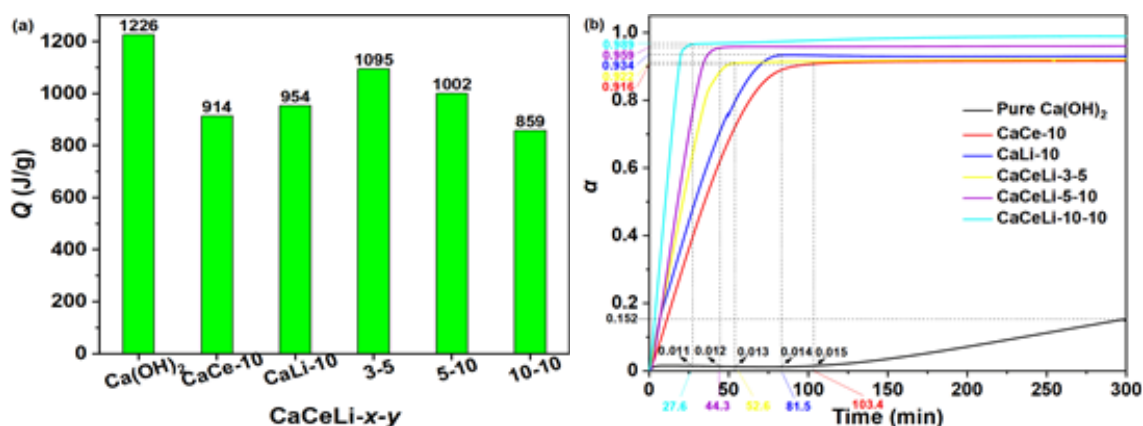

Fig. 1: (a) DSC curves of Ca(OH)$_2$ and CaCeLi-x-y. (b) dehydration-temperature changes of CaCeLi-x-y with contents.

Additionally, integrating the dehydration peaks of DSC curves gives the dehydration heat (Q), which is an index of the energy density. The trend in Q values reasonably drops from 1223 J/g to 859 J/g with increasing amounts of Ce(NO$_3$)$_3$ and LiOH (Fig. 2a).

Heat-storage kinetics

The effect of Ce(NO$_3$)$_3$ and LiOH on the thermal storage of Ca(OH)$_2$ can be further examined with isothermal dehydration methods using TG technology. The samples are heated at 20 °C/min until 310 °C, this temperature is then maintained for 300 min, and the weight loss is recorded. The conversion (a) is calculated with $(m_0 - m_t)/m_{H2O}$ (m_t is the sample mass at time t/min, m_{H2O} is the theoretical mass of water in the sample, and m0 is the initial mass of the sample). Figure 2b shows the relationship between a of the isothermal dehydration and the heat-storage time (t/min).
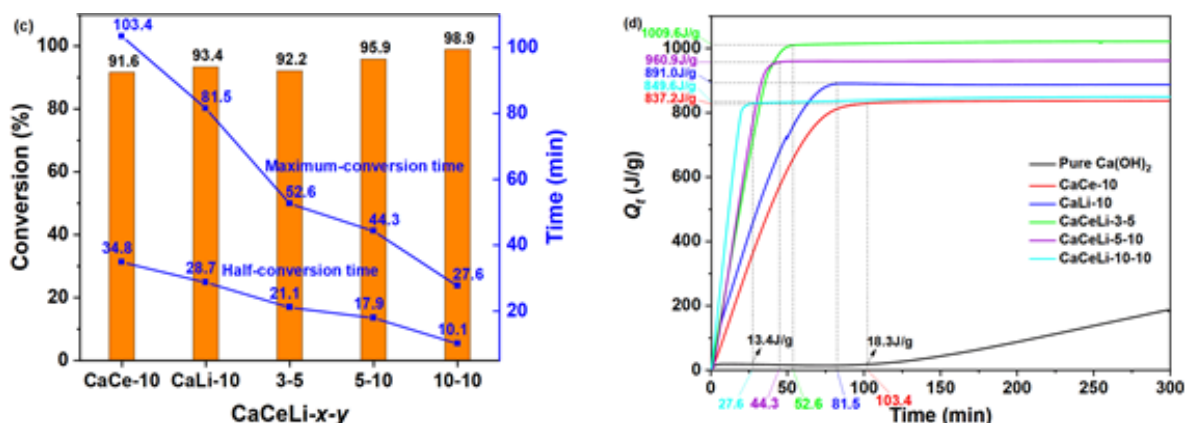
Fig. 2: (a) Dehydration heat (*Q*) values of Ca(OH)$_2$ and CaCeLi-*x-y* composites. (b) Isothermal dehydration curves of pure Ca(OH)$_2$ and CaCeLi-*x-y* composite at 310 °C. (c) Maximal and relative conversion time for Ca(OH)$_2$ and CaCeLi-*x-y* composites at 310 °C. (d) Relationships between the stored heat (*Q$_t$*) and time *t* (min) for Ca(OH)$_2$ and CaCeLi-*x-y* composites at 310 °C.

The curve of pure Ca(OH)$_2$ shows a storage process which is rather slow and an induction period of about 100 min with α <1.5%. However, for all of the CaCeLi-*x-y* composites, the conversion rises sharply without any induction period (Fig. 2b). At 310 °C, the half-conversion times ($\tau_{0.5}$) of CaCeLi-*x-y* composites are 21, 18, and 10 min for CaCeLi-3-5, CaCeLi-5-10, and CaCeLi-10-10, respectively. This is quicker than the corresponding times for CaCe-10 and CaLi-10 (34.8 and 28.7 min). The maximum conversions (α_{max}) increase by 92%, 95%, and 98% along with the corresponding maximum-conversion time (t_{max}) of 52.6, 44.3, and 27.6 min for CaCeLi-3-5, CaCeLi-5-10, and CaCeLi-10-10, respectively. Moreover, the two-component composites of CaCe-10 and CaLi-10 show 91.6% and 93.4% α_{max} with the respective t_{max} of 103.4 and 81.5 min. In terms of Ca(OH)$_2$, the conversion is only 1.5% in 103.4 min. In contrast, these values exhibit better performance than that shown by respective ZrO(NO$_3$)$_2$-Ca(OH)$_2$[27], KNO$_3$-Ca(OH)$_2$ [19, 20], and BN-Ca(OH)$_2$ [23] for energy storage. Thus, both the increase in α_{max} and the decrease in t_{max} are exceptional and much better than what was revealed by the single addition of Ce(NO$_3$)$_3$ and LiOH. These data confirm that the conversion can be improved by 65.3-fold in 30 min and it is difficult to store energy using pure Ca(OH)$_2$ at 310 °C.

$$Q_t = Q\,\alpha_t \quad (2)$$

$$v_Q = \frac{dQ}{dt} = \frac{Q_t}{t} \quad (3)$$

where α_t is the dehydration conversion in time *t*/min, *Q* is the dehydration reaction heat of the relative materials, Q_t (J·g^{-1}) is the heat stored in composites in time *t*/min, and v_Q (J·g^{-1}·min^{-1}) is the heat-storage rate at time *t*/min.

Using the DSC data and isothermal α_t, Q_t was calculated by Eq. 2 and the Q_t–*t* relationships are shown in Fig. 2d. At 310 °C, the maximal stored heat values (Q_{max}) are 1009.6, 960.9, 849.6, 891.0, and 837.2 J/g, stored by CaCeLi-3-5, CaCeLi-5-10, CaCeLi-10-10, CaLi-10, and CaCe-10 in 52.6, 44.3, 27.6, 81.5, and 103.4 min, respectively. The average heat-storage rates (v_Q) were calculated according to Eq. (3). The v_Qs of CaCeLi-3-5, CaCeLi-5-10, CaCeLi-10-10, CaLi-10, and CaCe-10 are 19.2, 21.7, 30.8, 10.9, and 8.1 J/(g·min), respectively. However, the Q_t measured for pure Ca(OH)$_2$ is only 18.3 J/g in the first period of 103 min and the v_Q was calculated to be 0.18 J/(g·min). Therefore, compared to pure Ca(OH)$_2$, the heat-storage rate of CaCeLi-10-10 increases by 173.3-fold. The three-component composites are better than the two-component composites. Both the heat-storage rate and the conversion ratio of Ca(OH)$_2$ are massively enhanced by co-doping with Ce(NO$_3$)$_3$ and LiOH. These results also demonstrate that both the v_Q and α increase with increasing amounts of these two additives.

Reversibility of heat storage and heat release
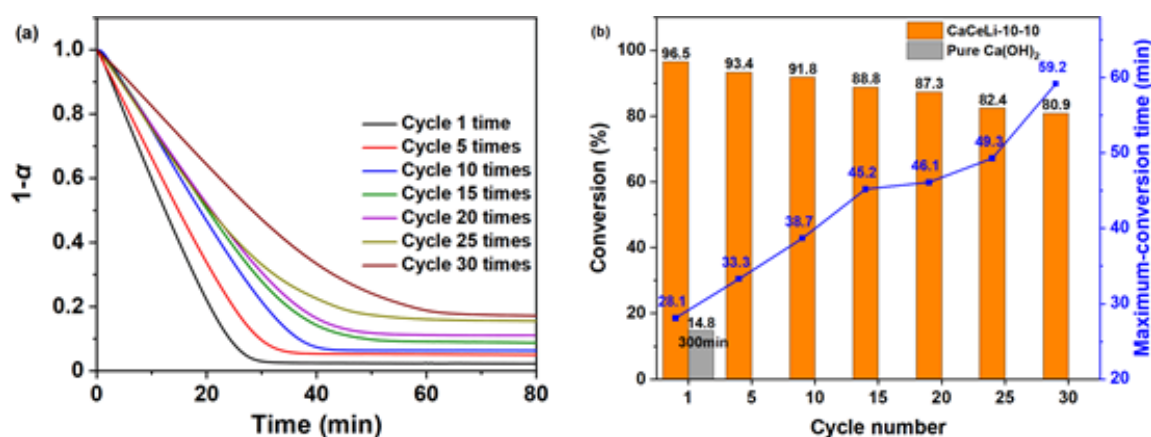
Fig. 3: (a) Conversion times for different numbers of cycles. (b) Relationships between both maximum conversion and conversion time and dehydration–rehydration cycle number of pure Ca(OH)$_2$ and CaCeLi-10-10.

The reversibility of dehydration–rehydration cycles is an essential index to evaluate the efficiency of heat-storage materials. The CaCeLi-10-10 composite was chosen to conduct dehydration–hydration cycles. Dehydration of CaCeLi-10-10 (5.0 g) was performed at 310 °C in 2 h and the hydration was carried out at around 50 °C. During cycling, samples were collected for running isothermal dehydration to reveal the maximal conversions and the corresponding times. The results are shown in Fig. 3. A 96% conversion is achieved in 28 min after the first cycle. After 20 and 30 cycles, the conversions are still 87% and 81% reached in 49 and 60 min, respectively. Therefore, the cycling stability of Ca(OH)$_2$ heat storage and heat release is significantly improved by co-doping Ce(NO$_3$)$_3$ and LiOH. CaCeLi-*x-y* composites are promising materials for large-scale applications.

Energy-storage models

Kinetic models of thermal storage are useful for computer simulation in engineering. According to the recommendations of the Kinetics Committee of the International Confederation for Thermal Analysis and Calorimetry [29], the kinetic control equation of the non-isothermal process for a gas–solid reaction can be described as per Eq. 4 [30-32].

$$\frac{d\alpha}{dT} = \frac{A}{\beta} \exp\left(-\frac{E}{RT}\right) f(\alpha) \qquad (4)$$

where α is a conversion, A is the pre-exponential factor (s^{-1}), E is the activation energy (kJ/mol), β is the heating rate (K/min), T is the temperature (K), R is the ideal gas molar constant (J/(mol·K)), and $f(\alpha)$ is the kinetic mechanism function of the dehydration reaction.

With the commonly used Archar–Brindley–Sharp–Wendworth (ABSW) differential method, Coats–Redfern (C–R) integral method (SI, Eq. 2 and 3), and average Rs values, the kinetic parameters of A and E as well as the mechanism function $f(\alpha)$ and $g(\alpha)$ can be derived. The most reasonable mechanism $f(\alpha)$ and $g(\alpha)$ for the dehydration reactions was clarified to be contracting cylinder (R2) as per Eq. 5 by the largest average Rs values derived from TG data at heating rates of 5, 7, and 10 °C/min (SI, Tables 3 and 4) [27,33].

$$G(\alpha) = 1-(1-\alpha)^{1/2} , \quad f(\alpha) = 2(1-\alpha)^{1/2} \qquad (5)$$

On the bases of model R2 and the C-R and ABSW methods, activation energy E and the pre-exponential factor A were obtained from the intercept and the slope of the ordinary least squares (OLS) linear regression of the TG data (SI, Fig. 2–4). The E and ln$A$ are listed in Table 2 and 3 for the dehydration of Ca(OH)$_2$ and CaCeLi-10-10, respectively. For the dehydration of pure Ca(OH)$_2$, the mean values of E and ln$A$ were calculated to be 202.11±7.92 kJ/mol and 34.03±1.54 s^{-1}, respectively. For CaCeLi-10-10 dehydration, the mean values are 132.54±2.85 kJ/mol and 24.05±0.46 s^{-1}. Thus, both kinetics parameters of E and ln$A$ are significantly reduced, by 34.6% and 29.4%, respectively; the energy barrier of heat storage is remarkably decreased. These results can possibly explain the 173.3-fold increase in heat-storage rate by the co-doped Ce(NO$_3$)$_3$ and LiOH. In addition, these number are all larger than that shown by the single addition of lithium and zirconium [27,31].

Table 2: Kinetic parameters for the dehydration process of Ca(OH)$_2$ using model R2

β/(°C·min^{-1})	C-R integral method			ABSW differential method		
	E/(kJ·mol^{-1})	ln(A/s)	Rs	E/(kJ·mol^{-1})	ln(A/s)	Rs
5	176.23	27.65	0.9996	208.52	36.69	0.9987
7	187.75	33.25	0.9998	215.44	35.78	0.9984
10	195.35	32.59	0.9999	229.37	38.19	0.9997
mean	186.44	31.16	–	217.78	36.89	–

**Table 3:** Kinetic parameters for the dehydration of CaCeLi-10-10 using model R2

β/(°C·min^{-1})	C-R integral method			ABSW differential method		
	E/(kJ·mol^{-1})	ln(A/s)	Rs	E/(kJ·mol^{-1})	ln(A/s)	Rs
5	139.93	25.03	0.9998	133.07	25.25	0.9985
7	134.54	23.55	0.9997	129.01	23.82	0.9997
10	138.05	24.47	0.9995	120.64	22.20	0.9998
mean	137.51	24.35	–	127.57	23.76	–

With these kinetic parameters and Eq. 4 and 5, kinetic equations for heat storage of pure Ca(OH)$_2$ and CaCeLi-*x-y* composites can be configured as per Eq. 6 and 7, respectively.

$$\frac{d\alpha}{dt} = 5.98 \times 10^{14} \times \exp\left(-\frac{2.02 \times 10^5}{RT}\right) \times 2 \times (1-\alpha)^{1/2} \quad (6)$$

$$\frac{d\alpha}{dt} = 2.79 \times 10^{10} \times \exp\left(-\frac{1.32 \times 10^5}{RT}\right) \times 2 \times (1-\alpha)^{1/2} \quad (7)$$

To evaluate the feasibility of this kinetic equation, the α values calculated by TG data at β = 2 °C /min are plotted as dots in Figures 4a and 4b for Ca(OH)$_2$ and CaCeLi-10-10 dehydration, respectively. The data calculated from Eq. 6 and 7 are plotted and fitted in lines in Fig. 4. The largest deviation between the experimental and Eq. 6 values for Ca(OH)$_2$ is 3.8%. The maximal divergence for the dehydration of CaCeLi-10-10 is 8.5%, which is acceptable. Thus, this kinetic equation (Eq. 7) is feasible for simulations and reactor design.
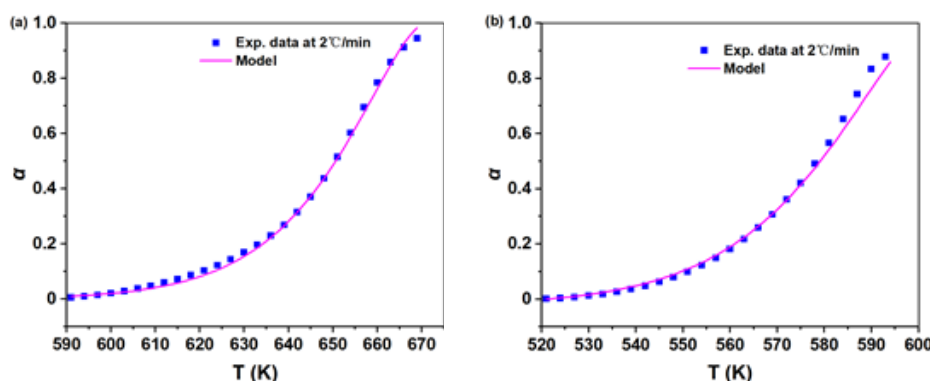
Fig. 4: Comparison between TG data and the model-calculated data for the dehydration processes of (a) pure Ca(OH)$_2$ and (b) CaCeLi-10-10 composite.

X-ray diffraction and X-ray photoelectron analysis

CaCeLi-10-10 and its dehydration–hydration product were characterized by X-ray diffraction (XRD) to determine the composition and microstructure. Besides peaks (2θ =17.98°, 28.62°, 34.06°, 47.06°, 50.74°, 54.28°, 56.12°, 59.33°, 62.60°, 64.28°, 71.74°, 77.75°, and 79.11°) attributed to $Ca(OH)_2$ (PDF 78-0315), an XRD pattern of CaCeLi-10-10 also shows peaks at 2θ, 24.76°, 32.16°, 35.72°, and 42.36° (Fig. 5a), which can be assigned to $Ce(NO_3)_3$ (PDF 16-0196). Signals of 2θ, 16.36°, 21.38°, 30.78°, 31.78°, and 36.78°, can be identified to $LiOH·H_2O$ (PDF 74-1820) in the XRD pattern of all composites examined (Fig. 5). For the dehydration and cycling products, 2θ signals at 33.22°, 47.60°, 56.44°, 59.20°, 69.50°, and 76.80° are attributed to CeO_2 (PDF 81-0792) (Fig. 5c and 5d) and also correspond to (200), (220), (311), (222), (311), (400), and (331) crystal planes indexed to the cubic fluorite structure of CeO_2. CeO_2 should be generated from $Ce(NO_3)_3$ decomposition during the heat storage (Eq. 8). This species is also revealed by XPS and HRTEM data (Figs. 6 and 10).
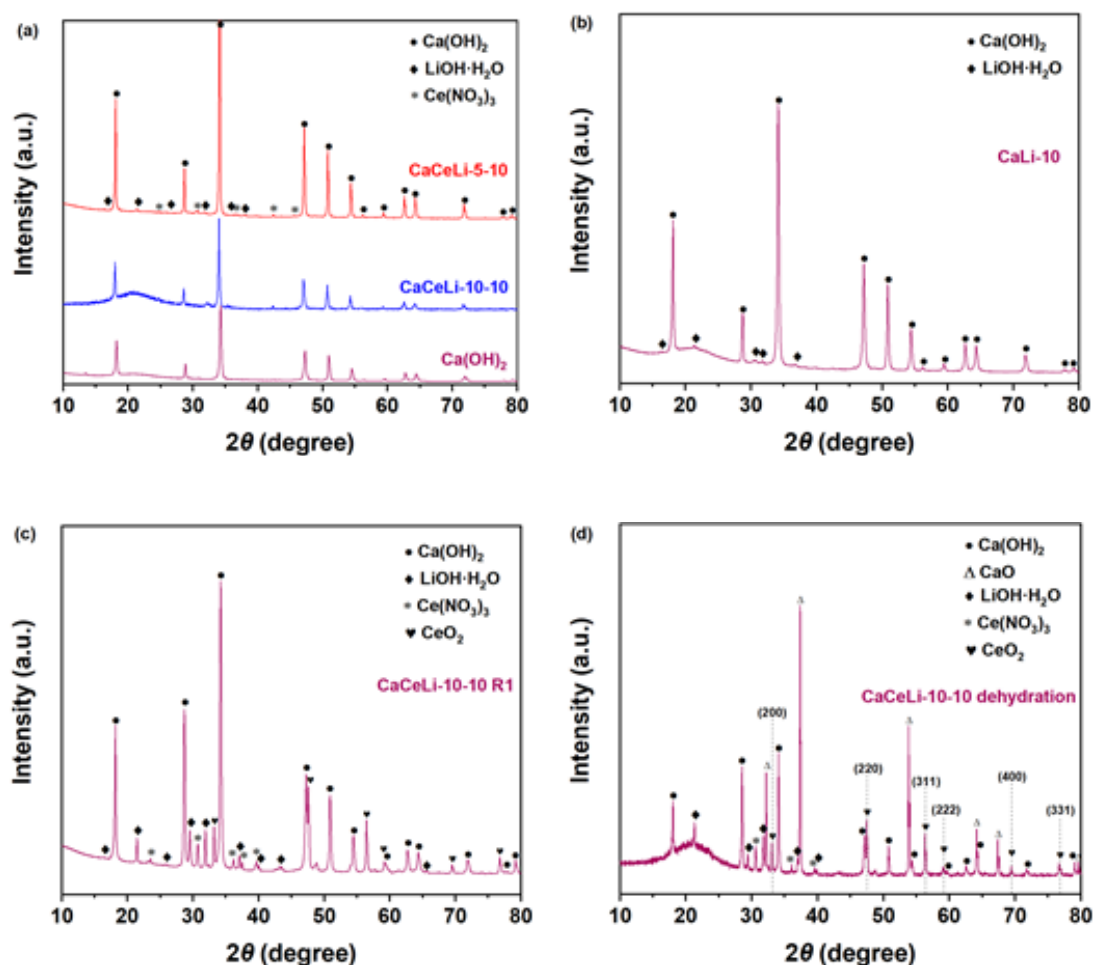
Fig. 5: X-ray diffraction patterns of samples from (a) CaCeLi-5-10, CaCeLi-10-10, and $Ca(OH)_2$; (b) CaLi-10; (c) CaCeLi-10-10 after one dehydration–hydration cycle; (d) dehydration products of CaCeLi-10-10.

$$2 \, Ce(NO_3)_3 = 2 \, CeO_2 + 6 \, NO_2 + O_2, \quad (8)$$
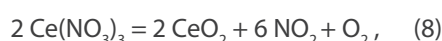
$$2d_{hkl}\sin\theta = n\lambda, \quad (9)$$

$$d_{hkl} = [4/3(h^2+hk+k^2)a^{-2}+l^2c^{-2}]^{-1/2}, \quad (10)$$

$$V = 1.732 \times a^2 \times c/2, \quad (11)$$

On the bases of XRD data, the lattice parameters and unit cell volumes of $Ca(OH)_2$ were calculated using Eq. 9–11, and (001), (011), (012), and (110) crystal planes (Table 4). Doping solely with $LiOH·H_2O$, the data indicate that the parameters are increased although the ionic radius of Li^+ (0.72 Å) is less than that of Ca^{2+} (ionic radius 0.99 Å) (Entry 2 vs 1), which may indicate that $LiOH·H_2O$ lies mainly in the interlayers of $Ca(OH)_2$ rather than the replacement of Ca^{2+}. This accords with other results reported in the literature.[33] With the

addition of $Ce(NO_3)_3$, both the lattice parameters and the volumes are further enlarged (Entries 1–4). The volume is increased by 2.05% by doping 10 wt% $Ce(NO_3)_3$ and 10 wt% $LiOH \cdot H_2O$. After dehydration-hydration cycles, results show that the parameters and volume become less than those of its precursor but still larger than those of pure $Ca(OH)_2$ (Entries 5 vs 4 and 1). Notably, the Ce^{3+} (radius, 1.03 Å) is changed into

CeO_2 during the dehydration process (Eq. 8, Fig. 6 and 9). This increase could be induced by the large volume of CeO_2 lying in the crystalline layers of $Ca(OH)_2$. This shrinkage might occur because of the strong affinity of CeO_2 to the surrounding OH^- groups of $Ca(OH)_2$ (I and II, Fig. 7). Further, lattice parameter expansion destabilizes crystalline $Ca(OH)_2$ and readily results in dehydration and a lower dehydration temperature (Fig. 1).

Table 4: Lattice parameters and lattice volumes of $Ca(OH)_2$ in composites

Entry	Sample	a(Å)	b(Å)	c(Å)	V(Å³)
1	$Ca(OH)_2$	3.5812	3.5812	4.8791	54.1901
2	CaLi-10	3.5897	3.5897	4.8973	54.6494
3	CaCeLi-5-10	3.5909	3.5909	4.9012	54.7302
4	CaCeLi-10-10	3.5953	3.5953	4.9225	55.1039
5	CaCeLi-10-10-R1	3.5857	3.5857	4.8877	54.4223
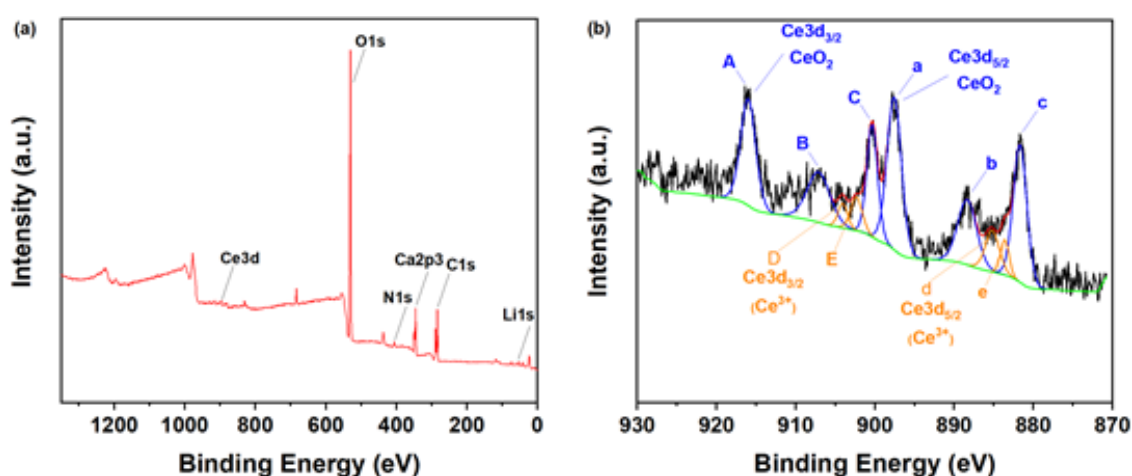
Fig. 6: (a) XPS elemental survey spectra of dehydration products of CaCeLi-10-10. (b) XPS spectra of Ce $3d_{3/2}$ and Ce $3d_{5/2}$.

In addition, the dehydration product of CaCeLi-10-10 was further analyzed by X-ray photoelectron spectra (XPS). In those spectra, some signals can be attributed to Ce 3d, Ca 2p, O 1s, and Li 1s, respectively (Fig. 6). The complicated XP spectra of ceria predominantly resulted from the hybridization of the Ce 4f with the O 2p (Fig. 6b). The two-group peaks of A, B, C, D, and E as well as a, b, c, d, and e are assigned to Ce $3d_{3/2}$ and Ce $3d_{5/2}$ spin–orbit energy states, respectively. The A–a doublet is formed by the primary photoemission from CeO_2; namely,

O $2p^6$, Ce $3d^9$ $4f^0$. The B–b and C–c doublets are also formed from CeO_2 owing to the electron (one or two) transfer from O 2p filled orbitals to Ce 4f empty orbitals; namely O $2p^4$, Ce $3d^9$ $4f^2$ and O $2p^5$, Ce $3d^9$ $4f^1$, respectively. The weak D–d and E–e doublets can be ascribed to photoemission from Ce^{3+}. These remarkably weak signals of D, d, E, and e mean that the Ce^{3+} contents are much less. The intense signal at 881.68 eV corresponding to Ce^{4+} clarifies that CeO_2 is a main species (Eq. 8),[34] which accords with the XRD data (Fig. 5). This BE

value 881.68 eV is notably less than 882.9 eV assigned to the main signal of the pure CeO_2. The value decrease indicates the electron-density increase of Ce^{4+}. This increase should be a function of both the high electrophilicity of Ce^{4+} and the electron donation of the surrounding OH^- groups. An intense peak of O 1s at 531.0 eV can be assigned to the OH group. [36] Thus, the action of CeO_2 on $Ca(OH)_2$ could probably be presented as a strong interaction between CeO_2 and the OH group, which promotes the formation of a water molecule to yield the dehydration product CaO.

Scanning electron microscopy

The particle size and agglomeration of the CaCeLi-*x-y* composite were examined by scanning electron microscopy (SEM) (Fig. 8). Strong agglomeration and irregular layer particles are observed in Fig. 7a for pure $Ca(OH)_2$ after one dehydration–hydration cycle. Figures 7b–7d show the morphologies of the dehydration products of CaCeLi-3-5,

CaCeLi-5-10, and CaCeLi-10-10. It can be seen that these particle sizes tend to be less than 10 μm and the size decreases unambiguously with the increasing contents of $Ce(NO_3)_3$ and LiOH. These results indicate that these additives are beneficial for reducing particle size and agglomeration. In contrast to Figure 7a, Figure 7e also shows smaller size particles that is for the sample from one dehydration–hydration cycle of CaCeLi-10-10. These sphere particles should result from the additives. After 20 cycles of CaCeLi-10-10, the particle size becomes larger than that of one cycle (Fig. 7f vs 7e). This increase in size might indicate that the shell formed by CeO_2 and LiOH on the surface of hydrated lime particles becomes more incomplete as the cycle increase (Fig. 8). These results may partially elucidate that the conversion decreases with increasing cycles, as depicted in Fig. 3 (α change from 96.5% to 80.9%). Accordingly, $Ce(NO_3)_3$-LiOH cooperation renders the materials with huge heat storage efficiency through catalyzation and optimizing the microstructure, i.e., improving permeability and stability, and reducing agglomeration.
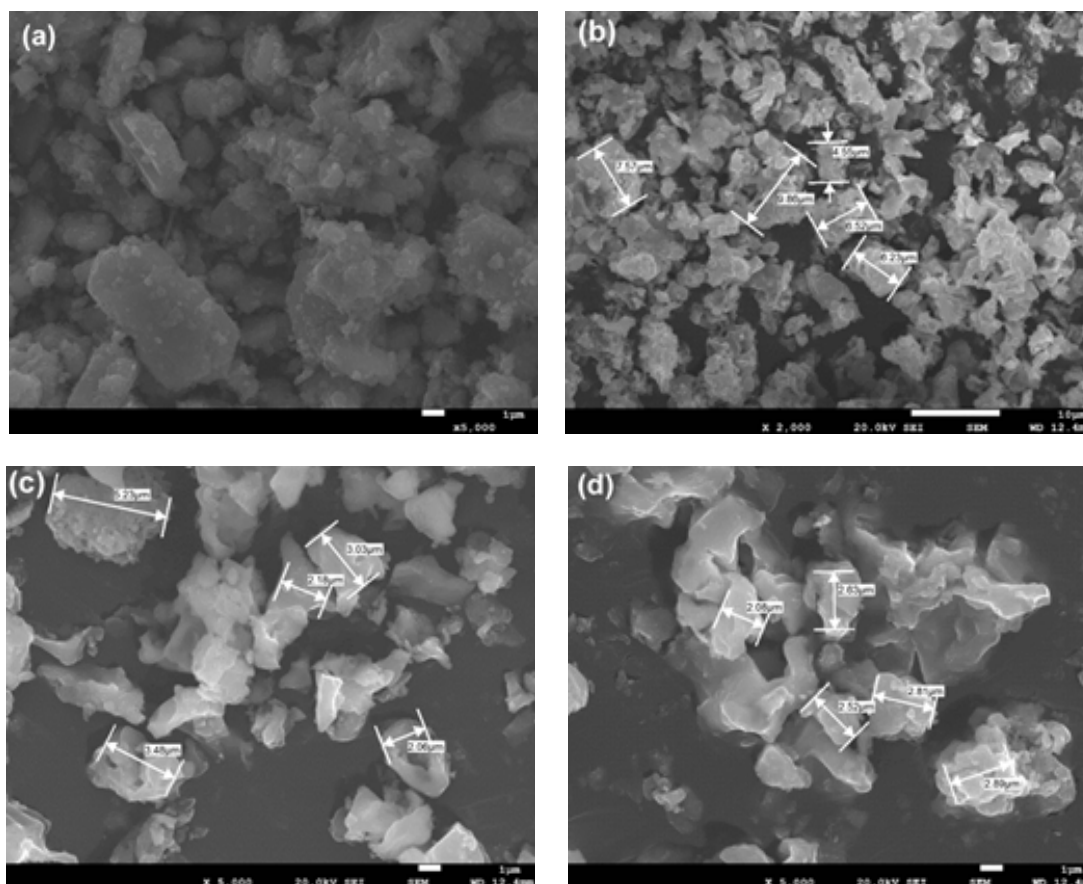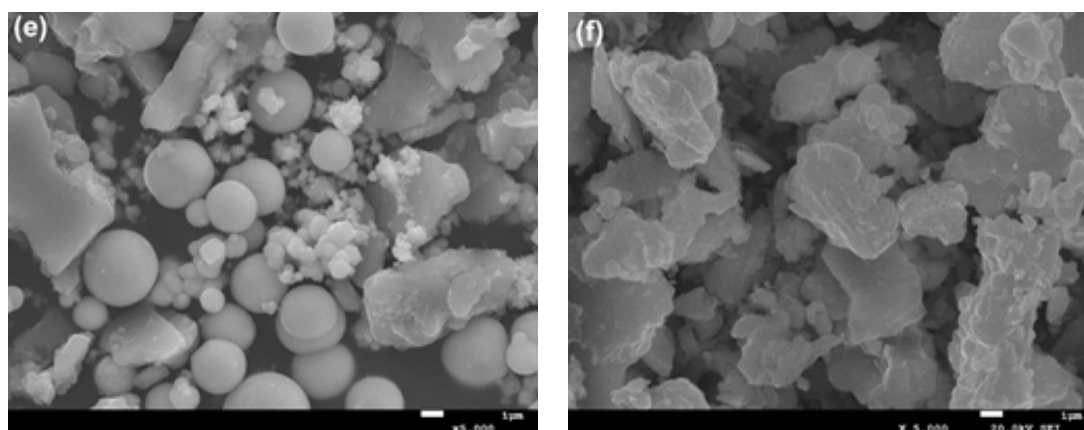
Fig. 7: SEM images of samples from (a) pure Ca(OH)$_2$ after one cycle; (b) dehydration product of CaCeLi-3-5; (c) dehydration product of CaCeLi-5-10; (d) dehydration product of CaCeLi-10-10; (e) CaCeLi-10-10 after one cycle; (f) CaCeLi-10-10 after 20 cycles.

High resolution transmission electron microscopy
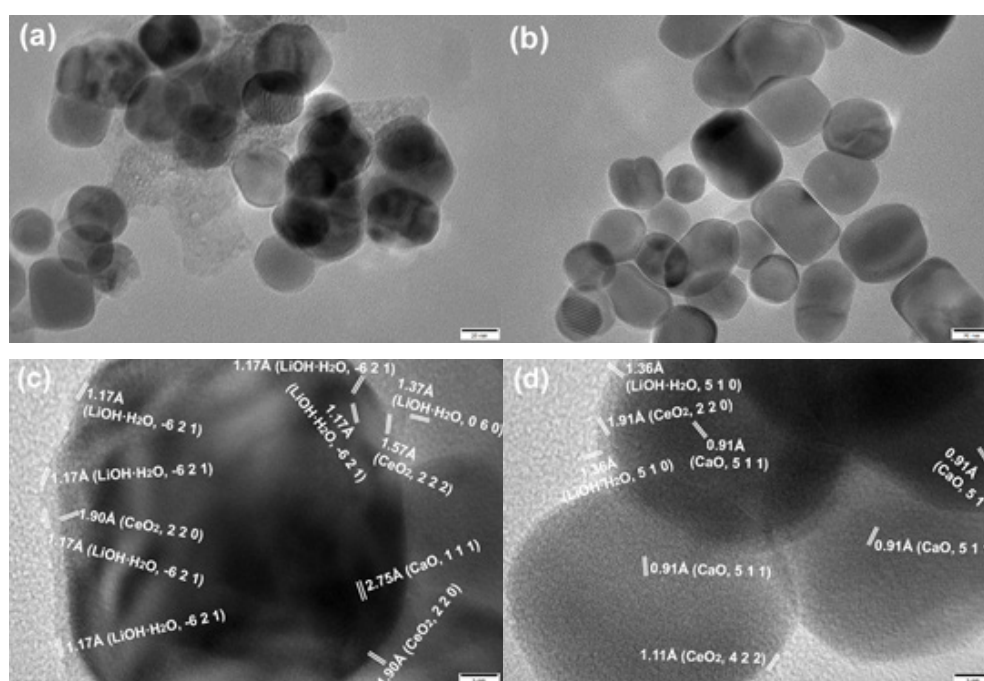
Fig. 8: HRTEM images of samples from the dehydration of CaCeLi-10-10.

Moreover, the material is further identified with high resolution transmission electron microscopy (HRTEM). Nanoparticles from the dehydration of CaCeLi-10-10 are shown in Figure 8, in which a number of crystal planes can be clearly identified. Specifically, the interplanar spacing and planes of 1.17 Å (-621) and 1.37 Å (060) can be assigned to crystalline LiOH·H$_2$O. The interplanar distances and planes, 1.11 Å (422), 1.35 Å (400), 1.57 Å (222), and 1.90(1) Å (220), are attributed to the cubic fluorite structure of CeO$_2$ [33]. Some of these planes agree well with the XRD data of CeO$_2$, i.e., 2θ = 69.50°, 59.20°, and 47.60° (Fig. 5d). The distances and planes of 0.91 Å (511) and 2.75 Å (111) belong to CaO. Therefore, these results reveal that some crystal LiOH·H$_2$O and CeO$_2$ deposit on the surface of Ca(OH)$_2$ and limit the particle size and agglomeration by covering the OH groups of Ca(OH)$_2$ because the multilayer formation and agglomeration result from the hydrogen bonds among OH groups [37].

CONCLUSION

It is demonstrated that $Ce(NO_3)_3$ and LiOH cooperation significantly decreases the dehydration temperature and the heat-storage time of $Ca(OH)_2$. At 310 ℃, the addition of 10 wt% $Ce(NO_3)_3$ and 10 wt% LiOH improves the conversion and heat-storage rate by 65.3- and 173-fold, respectively. The reversibility of materials in dehydration–rehydration cycles is also significantly enhanced. Kinetic equations for the dehydration were derived and could be leveraged in future for the purpose of informing reactor design and simulations. The activation energy E and pre-exponential factor ln$A$ for $Ca(OH)_2$ dehydration can be reduced by 34.6% and 29.4%, respectively. HRTEM, XRD, and XPS data provide insights regarding the mechanism of action of these additives. SEM images show that the particle size and aggregation are notably diminished. Thus, $Ca(OH)_2$-$Ce(NO_3)_3$-LiOH composites have significant potential as materials for chemical heat storage in large-scale applications.

CONFLICTS OF INTEREST

There are no conflicts to declare.

REFERENCES

1. Awan AB, Zubair M, Praveen RP, Bhatti AR. (2019). Design and comparative analysis of photovoltaic and parabolic trough based CSP plants. Solar Energy. 183:551-565.

2. Carrillo AJ, Gonzalez-Aguilar J, Romero M, Coronado JM. (2019). Solar Energy on Demand: A Review on High temperature thermochemical heat storage systems and materials. Chem Rev. 119:4777-4816.

3. Liu M, Tay NHS, Bell S, Belusko M, Jacob R, et al. (2016). Review on concentrating solar power plants and new developments in high temperature thermal energy storage technologies. Renew Sustain Energy Rev. 53:1411-1432.

4. Gonzalez-Roubaud E, Perez-Osorio D, Prieto C. (2017). Review of commercial thermal energy storage in concentrated solar power plants: Steam vs. molten salts. Renew Sustain Energy Rev. 80:133-148.

5. Achkari O, El Fadar A. (2020). Latest developments on TES and CSP technologies - Energy and environmental issues, applications and research trends. Appl Therm Eng. 167:114806.

6. Alva G, Lin Y, Fang G. (2018). An overview of thermal energy storage systems. Energy. 144:341-378.

7. Dincer I. (2002). On thermal energy storage systems and applications in buildings. Energy Buildings. 34:377-388.

8. Wei GS, Wang G, Xu C, Ju X, Xing LJ, et al. (2018). Selection principles and thermophysical properties of high temperature phase change materials for thermal energy storage: A review. Renew Sustain Energy Rev. 81:1771-1786.

9. Prasad JS, Muthukumar P, Desai F, Basu DN, Rahman MM. (2019). A critical review of high-temperature reversible thermochemical energy storage systems. Appl Energy. 254:113733.

10. Pardo P, Deydier A, Anxionnaz-Minvielle Z, Rouge S, Cabassud M, et al. (2014). A review on high temperature thermochemical heat energy storage. Renew Sustain Energy Rev. 32:591-610.

11. Dizaji HB, Hosseini H. (2018). A review of material screening in pure and mixed-metal oxide thermochemical energy storage (TCES) systems for concentrated solar power (CSP) applications. Renew Sustain Energy Rev. 98:9-26.

12. Prasad JS, Muthukumar P, Desai F, Basu DN, Rahman MM. (2019). A critical review of high-temperature reversible thermochemical energy storage systems. Appl Energy. 254:113733.

13. Song C, Liu XL, Zheng HB, Bao C, Teng L, et al. (2021). Decomposition kinetics of Al- and Fe-doped calcium carbonate particles with improved solar absorbance and cycle stability. Chem Eng J. 406:126282.

14. Yan T, Wang RZ, Li TX, Wang LW, Fred IT. (2015). A review of promising candidate reactions for chemical heat storage. Renew Sustain Energy Rev. 43:13-31.

15. Pardo P, Anxionnaz-Minvielle Z, Rouge S, Cognet P, Cabassud M. (2014). $Ca(OH)_2$/CaO reversible reaction in a fluidized bed reactor for thermochemical heat storage. Solar Energy. 107:605-616.

16. Angerer M, Becker M, Harzschel S, Kroper K, Gleis S, et al. (2018). Design of a MW-scale thermo-chemical energy storage reactor. Energy Reports. 4:507-519.

17. Almendros-Ibanez JA, Fernandez-Torrijos M, Diaz-Heras M,

Belmonte JF, Sobrino C. (2019). A review of solar thermal energy storage in beds of particles: Packed and fluidized beds. Solar Energy. 192:193-237.

18. Yuan Y, Li Y, Zhao J. (2018). Development on thermochemical energy storage based on CaO-based materials: A Review. Sustainability. 10:2660.

19. Andre L, Abanades S. (2020). Recent advances in thermochemical energy storage via solid-gas reversible reactions at high temperature. Energies. 13:5859.

20. Shkatulov A, Aristov Y. (2015). Modification of magnesium and calcium hydroxides with salts: An efficient way to advanced materials for storage of middle-temperature heat. Energy. 85:667-676.

21. Shkatulov A, Aristovab Y. (2017). Calcium hydroxide doped by KNO_3 as a promising candidate for thermochemical storage of solar heat. Rsc Adv. 7:42929-42939.

22. Yan J, Zhao CY. (2014). First-principle study of $CaO/Ca(OH)_2$ thermochemical energy storage system by Li or Mg cation doping. Chem Eng Sci. 117:293-300.

23. Huang C, Xu M, Huai X. (2019). Experimental investigation on thermodynamic and kinetic of calcium hydroxide dehydration with hexagonal boron nitride doping for thermochemical energy storage. Chem Eng Sci. 206:518-526.

24. Mejia AC, Afflerbach S, Linder M, Schmidt M. (2020). Experimental analysis of encapsulated $CaO/Ca(OH)_2$ granules as thermochemical storage in a novel moving bed reactor. Appl Therm Eng. 169:114961.

25. Criado YA, Alonso M, Abanades JC. (2016). Enhancement of a $CaO/Ca(OH)_2$ based material for thermochemical energy storage. Solar Energy. 135:800-809.

26. Funayama S, Takasu H, Kim ST, Kato Y. (2020). Thermochemical storage performance of a packed bed of calcium hydroxide composite with a silicon-based ceramic honeycomb support. Energy. 201:117673.

27. Li YT, Li MT, Xu ZB, Meng ZH, Wu QP. (2020). Dehydration kinetics and thermodynamics of $ZrO(NO_3)_2$-doped $Ca(OH)_2$ for chemical heat storage. Chem Eng J. 399:125841.

28. Yan J, Zhao CY, Xia BQ, Wang T. (2019). The effect of dehydration temperatures on the performance of the $CaO/Ca(OH)_2$ thermochemical heat storage system. Energy. 186:115837.

29. Vyazovkin S, Burnham AK, Criado JM, Perez-Maqueda LA, Popescu C, et al. (2011). ICTAC Kinetics Committee recommendations for performing kinetic computations on thermal analysis data. Thermochim Acta. 520:1-19.

30. Chen X, Jin X, Liu Z, Ling X, Wang Y. (2018). Experimental investigation on the $CaO/CaCO_3$ thermochemical energy storage with SiO_2 doping. Energy. 155:128-138.

31. Yan J, Zhao CY. (2015). Thermodynamic and kinetic study of the dehydration process of $CaO/Ca(OH)_2$ thermochemical heat storage system with Li doping. Chem Eng Sci. 138:86-92.

32. Long XF, Dai L, Lou B, Wu J. (2017). The kinetics research of thermochemical energy storage system $Ca(OH)_2/CaO$. Int J Energy Res. 41:1004-1013.

33. Li M-T, Li YT, Sun L, Xu ZB, Zhao Y, et al. (2021). Tremendous enhancement of heat storage efficiency for $Mg(OH)_2$-MgO-H_2O thermochemical system with addition of $Ce(NO_3)_3$ and LiOH. Nano Energy. 81:105603.

34. Maruyama A, Kurosawa R, Ryu J. (2020). Effect of lithium compound addition on the dehydration and hydration of calcium hydroxide as a chemical heat storage material. ACS Omega. 5:9820-9829.

35. Postole G, Postole G, Chowdhury B, Karmakar B, Pinki K, et al. (2010). Auroux A, Knoevenagel condensation reaction over acid-base bifunctional nanocrystalline $Ce_xZr_{1-x}O_2$ solid solutions. J Catal. 269:110-121.

36. Yu S, Wang XX, Liu YF, Chen ZS, Wu YH, et al. (2019). Efficient removal of uranium (VI) by layered double hydroxides supported nanoscale zero-valent iron: A combined experimental and spectroscopic studies. Chem Eng J. 365:51-59.

37. Xu M, Huai X, Cai J. (2017). Agglomeration behavior of calcium hydroxide/calcium oxide as thermochemical heat storage material: a reactive molecular dynamics study. J Phys Chem C. 121:3025-3033.